Parameter Estimation for Subsurface flow Using Ensemble Data Assimilation

S Ruchi and S Dubinkina
CWI, P.O. Box 94079, 1098 XG Amsterdam, The Netherlands
E-mail: s.ruchi@cwi.nl

Abstract

Over the years, different data assimilation methods have been implemented to acquire improved estimations of model parameters by adjusting the uncertain parameter values in such a way that the mathematical model approximates the observed data as closely and consistently as possible. However, most of these methods are developed on the assumption of Gaussianity, e.g. Ensemble Kalman Filters, which is not the case in practical situations, and hence they result in poor estimations. In this work, the estimations of uncertain parameters are acquired from an Ensemble Square Root Kalman Filter and from a novel method, an Ensemble Transform Particle Filter, that does not have an assumption of Gaussianity. The latter method is developed on the backbone of Bayesian approach of sequential Monte Carlo with the framework of linear transport problem and has proved to be highly beneficial for systems with non-Gaussian distributions. We examine the performance of these methods in a twin experiment setup, when the observations of pressure are synthetically created based on the assumed true values of the uncertain parameters and implementing the Darcy flow model as the forward model, which is used for the data assimilation algorithm as well. We consider two test cases based on different geometrical configurations and distributions of permeability field across the domain representing low and high dimensional systems with small and large number of uncertain parameters, respectively. The numerical experiments demonstrate that Ensemble Transform Particle Filter provides comparable results with that of Ensemble Square Root Kalman Filter for the low dimensional system and outperforms it for the high dimensional system.

Keywords: Bayesian inference, data assimilation, ensemble Kalman filter, particle filter, subsurface flow, parameter estimation.

1 Introduction

Accurate estimation of subsurface geological properties like permeability, porosity etc. is essential for many fields specially where such predictions can have large economic or environmental impact, for instance prediction of oil or gas reservoir locations. If we know these geological parameters and model variables of subsurface flow systems accurately enough, it becomes possible to solve a so-called forward model and predict the outcome of any action. However, these subsurface reservoirs are buried thousands of feet below the earth surface and exhibit a highly heterogeneous structure, which makes it difficult to obtain their geological parameters. Usually a prior information about the parameters is given, which still needs to be corrected by observations of pressure and production rates. These observations are, however, known only at the well locations that are often hundreds of meter apart and moreover are corrupted by errors. This gives us instead of a well-posed forward problem an ill-posed inverse problem of estimating uncertain parameters, since many possible combinations of parameters can result in equally good matches to the observations.

There exists a vast literature describing various techniques that have been implemented to solve such inverse problems and are generally termed as history matching methods in the field of reservoir modeling. Different inverse problem techniques for groundwater and petroleum reservoir have been developed and used by many researchers over the years, e.g. in [21] the authors implemented Markov chain Monte Carlo methods with different perturbation approaches and tested their performance on a 2-D reservoir model, [28] presented the implementation of Gauss-Newton method for estimation of reservoir parameters, [30, 5] showed the application of neighborhood algorithm which approximates the posterior distribution by partitioning the model parameter space into regions of roughly uniform distribution, [25] applied representer method to estimate states and parameters for a 1-D two-phase reservoir model.

This approach expands all the unknown variables using a finite sum of representer functions weighted by the representer coefficients. The representer function describes the influence of the corresponding measurement on the solution and the representer coefficients determines how strong each representer should be accounted for in the final solution. In [33] authors used Levenberg–Marquardt method to characterize reservoir pore pressure and permeability, [34, 7] reviewed methods for solving the output least-squares problem using gradient and sensitivity based techniques. A more detailed discussion of various history matching algorithm can be found in the review paper [20].

For reservoir models the term data assimilation and history matching are used interchangeably, as the goal of data assimilation is the same as that of history matching, where we use observations to improve a solution from a mathematical model by correcting uncertain parameters. Though data assimilation had originally been employed in the field of meteorology and oceanography for state prediction by correcting initial conditions [10], now-a-days it is one of the frequently employed approach for parameter estimation in subsurface flow models as well [22], since it can easily be extended to estimate model parameters by implementing the method of state augmentation [15]. The idea here is to expand the state space by adding the uncertain parameters so that parameters act as the model variables in the data assimilation system and the chosen assimilation algorithm can then be applied to the augmented system in a usual way.

Over the years considerable efforts have been devoted to develop robust data assimilation techniques which could provide better assessment of state at affordable computational costs. There are mainly two classes of methods in data assimilation: variational approach which is based on minimization of an appropriate cost functional subjected to model constraints providing a single estimate and ensemble approach which provides an ensemble of estimates whose variability can directly be used to evaluate the uncertainty.

Ensemble Kalman filters and particle filters are examples of ensemble based approaches. Ensemble Kalman filter was developed to handle non-linear models at low computational cost. It updates the model states based on the assumption of Gaussian probability distribution. There are different variations of ensemble Kalman filters which can be broadly divided into two categories namely: stochastic approach and deterministic approach. In stochastic approach random noise is added to the observations and in deterministic approach a linear transformation is used to update the ensemble members. Ensemble square root Kalman filter (EnSRF) is based on the later approach [31]. The advantage of EnSRF over the stochastic approach is that it does not introduce an additional error due to the perturbation.

Initial application of ensemble Kalman filters in the field of groundwater hydrology is used for soil moisture estimation and is demonstrated in [27]. In petroleum engineering, [17] presented the first implementation of ensemble Kalman filter using a dynamic two-phase model of fluid flow in a well. Since then it has been investigated by a variety of researchers in subsurface flow models, e.g. in [9] the authors demonstrated the use of ensemble Kalman filter for 2-D reservoir models. They tuned both dynamic variables (pressure and saturation) and static variables (permeability) providing improved estimations of permeability. In [3] both 2-D and 3-D models of a single phase flow were used to demonstrate the ability of ensemble Kalman filters to continuously update the hydraulic conductivity field and to study the effect of ensemble size, incomplete prior statistics and measurements. [1] presents a detailed review of the application of ensemble Kalman filter in reservoir engineering. As shown in these papers, the resulting updated ensemble for ensemble Kalman filters efficiently approximates the theoretical posterior distribution if the ensemble size is sufficiently large and the distributions are not far from Gaussian. Though, as the update equations are of the form of Kalman filter equation which corrects only the mean and covariance matrix, it limits the performance of EnKF for models with multimodal distributions, see [36, 6].

On the other hand, particle filters, also known as sequential Monte Carlo methods, seem to be quite promising for such physical systems. They are also ensemble based methods in which the probability density function is represented by a number of particles (also called samples or ensemble members) and their evolution is computed by solving the forward model for each particle. These particles are then assigned weights based on the information present in the observations of the true physical system. Particle filtering in its original form faces the issue of ensemble collapse after a few data assimilation steps and also struggles to represent the actual state of the physical systems if majority of the particles are far away from the observation. Due to these reasons particle filters were earlier assumed to be impractical for high-dimensional systems as they required a large number of particles making the process computationally very expensive. However, recent developments help to overcome these limitations by generating computationally efficient particle filtering methods for high-dimensional systems as discussed in details in the review paper [32]. This paper discusses the existing strategies to reduce the variance

in the weights in order to avoid ensemble collapse (particle degeneration). One of the most common methods among these strategies is resampling and can be performed in different ways, e.g. residual sampling, stochastic universal, Monte Carlo Metropolis-Hastings sampling etc. The basic idea here is to abandon the low weight particles while generating new particles using the density of high weighted particles and then uniformly dividing weight among them. There has been significant work done for parameter estimation using particle filters in the area of hydrology. In [19] the authors used a conceptual rainfall-runoff model to estimate the model parameters and state posterior distributions. In [35] the authors presented a comparison among ensemble Kalman filter and particle filters with two different resampling strategies for a rainfall-runoff forecast and found that as the number of particles increased the particle filters outperformed ensemble Kalman filter. [18, 11] demonstrated application of particle filters to correct the soil moisture state and estimate hydraulic parameters.

The disadvantage of resampling for parameter estimation is that it does not modify the high weight particles and in the process of throwing away the low weight particles we lose some important information regarding the parameter distribution. Another method to deal with the issue of ensemble collapse is coupling, it transforms all the particles using a transformation matrix based on a linear transport problem in such a way that all the particles end up with uniform weights. Ensemble transform particle filter (EnTPF) [26] is a novel method based on the coupling methodology which presents a deterministic approach to resampling, a discussion later in section 2.2. In this research work, our goal is to study the performance of EnTPF in solving the inverse problem of parameter estimation for steady state single phase Darcy flow model while using the results from the ensemble Kalman filter as a benchmark. We perform two numerical experiments using twin experiment setup namely: two layer with fault but with constant permeability across a layer, and two layer without fault but with spatially varying permeability across a layer. For both cases we assume the permeability field across the domain defines the uncertain parameters. Further, we discuss the limitations faced by these ensemble based data assimilation methods and how the techniques like *inflation* and *localization* affect their performance. This paper is organized as follows: in the section 2 we describe both the data assimilation methods for parameter estimation problems. Section 3 explains the forward model and the numerical scheme used to discretize the Darcy model in detail. In section 4 we discuss the numerical experiment set-up followed by the results for both test cases and section 5 concludes the findings of this research work.

2 Data assimilation methods

We implement ensemble square root Kalman filter and ensemble transform particle filter for estimating the parameters of subsurface flow. Both of these schemes are based on Bayesian framework. Assume we have an ensemble of M model states $\{\mathbf{z}_m\}_{m=1}^{M}$, then according to this framework, the posterior distribution, which is the probability distribution $\pi(\mathbf{z}_m|\mathbf{y}_{\text{obs}})$ of model state $\mathbf{z}_m$ given a set of observations $\mathbf{y}_{\text{obs}}$, can be estimated by the pointwise multiplication of the prior probability distribution $\pi(\mathbf{z}_m)$ of the model state $\mathbf{z}_m$ and the conditional probability distribution $\pi(\mathbf{y}_{\text{obs}}|\mathbf{z}_m)$ of the observations given the model state, which is also referred as the likelihood function,

$$\pi(\mathbf{z}_m|\mathbf{y}_{\text{obs}}) = \frac{\pi(\mathbf{y}_{\text{obs}}|\mathbf{z}_m)\pi(\mathbf{z}_m)}{\pi(\mathbf{y}_{\text{obs}})}.$$

The denominator $\pi(\mathbf{y}_{\text{obs}})$ represents the marginal of observations and can be expressed as:

$$\pi(\mathbf{y}_{\text{obs}}) = \sum_{m=1}^{M} \pi(\mathbf{y}_{\text{obs}}, \mathbf{z}_m) = \sum_{m=1}^{M} \pi(\mathbf{y}_{\text{obs}}|\mathbf{z}_m)\pi(\mathbf{z}_m),$$

which shows that $\pi(\mathbf{y}_{\text{obs}})$ is just a normalisation factor. For parameter estimation using data assimilation the model state $\mathbf{z}_m = \begin{bmatrix}\mathbf{P}_m & \mathbf{u}_m\end{bmatrix}^T$, it includes both model variable $\mathbf{P}_m$ and uncertain parameters $\mathbf{u}_m$ and a model is augmented by the trivial equation $\dot{\mathbf{u}}_m = 0$, where $\dot{\mathbf{u}}_m$ is the time derivative of $\mathbf{u}_m$.

2.1 Ensemble Square Root Kalman Filter

The concept of ensemble Kalman filter is based on the idea of using an ensemble of states to estimate the mean and the covariance matrix and propagating these ensemble members in parallel. Ensemble Kalman filter has several derivations depending on either stochastic or deterministic approach of generating analysis. The ensemble square root Kalman filter (EnSRF) in particular is based on the deterministic approach.

Assume we have an ensemble of M initial model states $\{\mathbf{z}_m^b\}_{m=1}^M$, where b refers to a background (prior) state, which are sampled from a chosen prior probability density function, then the ensemble Kalman filter estimate (or analysis) $\{\mathbf{z}_m^a\}_{m=1}^M$ is given by:

$$\begin{aligned}\mathbf{z}_m^a &= \mathbf{z}_m^b + \mathbf{K}(\mathbf{y}_{\text{obs}} - \mathbf{H}\mathbf{z}_m^b), \quad m = 1, \ldots, M, \\ \mathbf{C}^a &= \mathbf{C}^b - \mathbf{K}\mathbf{H}\mathbf{C}^b,\end{aligned} \tag{2.1}$$

where $\mathbf{C}$ is an error covariance matrix of either background (with superscript b) or analysis (with superscript a) and $\mathbf{K}$ is the Kalman gain matrix which is given by

$$\mathbf{K} = \mathbf{C}^b\mathbf{H}^T(\mathbf{H}\mathbf{C}^b\mathbf{H}^T + \mathbf{R})^{-1}.$$

Here $\mathbf{R}$ is the measurement error covariance and $\mathbf{H}$ is the observation operator which projects a model state $\mathbf{z}$ to the observation phase space. We assume the observation operator $\mathbf{H}$ to be linear, though it could be extended to nonlinear observation operator as well. The background error covariance is represented by an ensemble of model states using ensemble anomalies as

$$\mathbf{C}^b = \frac{1}{M-1}\mathbf{A}^b(\mathbf{A}^b)^T,$$

with $\mathbf{A}^b$ being the background ensemble anomalies defined as

$$\mathbf{A}^b = \begin{bmatrix}(\mathbf{z}_1^b - \bar{\mathbf{z}}^b) & (\mathbf{z}_2^b - \bar{\mathbf{z}}^b) & \ldots & (\mathbf{z}_M^b - \bar{\mathbf{z}}^b)\end{bmatrix},$$

where $\bar{\mathbf{z}}^b$ is the mean defined by

$$\bar{\mathbf{z}}^b = \frac{1}{M}\sum_{m=1}^{M}\mathbf{z}_m^b.$$

According to [31] EnSRF updates the ensemble anomalies using a transformation matrix $\mathbf{S}$ such that:

$$\mathbf{A}^a := \mathbf{A}^b\mathbf{S},$$

$$\mathbf{C}^a = \frac{1}{M-1}\mathbf{A}^b\mathbf{S}\mathbf{S}^T(\mathbf{A}^b)^T,$$

where $\mathbf{S}$ is an $M \times M$ matrix involving a square root and hence the name ensemble square root Kalman filter. For our numerical experiments we define $\mathbf{S}$ as

$$\mathbf{S} = \left[\mathbf{I} + \frac{1}{M-1}(\mathbf{H}\mathbf{A}^b)^T\mathbf{R}^{-1}\mathbf{H}\mathbf{A}^b\right]^{-1/2}, \tag{2.2}$$

where $\mathbf{I}$ is an identity matrix of size $M \times M$. This gives us the analysis using a Kalman update formula equivalent to (2.1)

$$\mathbf{z}_m^a = \mathbf{z}_m^b + \frac{1}{M-1}\mathbf{A}^b\mathbf{S}^2(\mathbf{H}\mathbf{A}^b)^T\mathbf{R}^{-1}(\mathbf{y}_{\text{obs}} - \mathbf{H}\mathbf{z}_m^b), \quad m = 1, \ldots, M.$$

To ensure that the anomalies of analysis remain zero centered we check whether $\mathbf{A}^a\mathbf{1} = \mathbf{A}^b\mathbf{S}\mathbf{1} = \mathbf{0}$, given $\mathbf{S}\mathbf{1} = \mathbf{1}$ and $\mathbf{A}^b\mathbf{1} = \mathbf{0}$, where $\mathbf{1}$ is a vector of size M given by $\mathbf{1} = \begin{bmatrix}1 & 1 & \ldots & 1\end{bmatrix}^T$.

2.2 Ensemble Transform Particle Filter

In particle filtering we represent the probability distribution function of the states using ensemble members (also called particles), as in ensemble Kalman filter. We start by assigning prior (background) weight w_m^b to the particles and then rescale the weights based on the observation by using the Bayes' formula as shown below,

$$w_m^a = \frac{w_m^b\pi(\mathbf{y}_{\text{obs}}|\mathbf{z}_m^b)}{\pi(\mathbf{y}_{\text{obs}})}, \tag{2.3}$$

where w_m^a is the new (analysis) weight, $\pi(\mathbf{y}_{\text{obs}}|\mathbf{z}_m^b)$ the likelihood and $\pi(\mathbf{y}_{\text{obs}})$ is the normalization factor. It is important to note here that particle filters *do not* change the state $\mathbf{z}$ of the system, they only modify the weight of particles. For any dynamical system these weights become non-uniform just after a few

data assimilation steps, with only one particle having all the weight, while all the other particles have weights closer to zero, causing degeneracy of the particle filter. In this case the entire statistics of the system gets influenced by just that one particle, which might be far away from the true state and hence does not represent the real state of the system. Moreover, since particle filters do not modify the ensemble members but only rescale the weights, a sophisticated perturbation needs to be implemented for parameter estimation in non-chaotic systems. To deal with these limitations, particle filter has been modified using for example a coupling methodology known as ensemble transform particle filter (EnTPF).

EnTPF looks for a coupling between two discrete random variables B_1 and B_2 so as to convert the ensemble members belonging to the random variable B_2 with probability distribution $\pi(B_2 = \mathbf{z}_m^b) = w_m^a$ to the random variable B_1 with uniform probability distribution $\pi(B_1 = \mathbf{z}_m^b) = 1/M$. The coupling between these two random variables is an $M \times M$ matrix $\mathbf{T}$ whose entries should satisfy

$$t_{mj} \geq 0, \quad m, j = 1, \ldots, M, \tag{2.4}$$

$$\sum_{m=1}^{M} t_{mj} = \frac{1}{M}, \quad j = 1, \ldots, M, \tag{2.5}$$

$$\sum_{j=1}^{M} t_{mj} = w_m^a, \quad m = 1, \ldots, M. \tag{2.6}$$

We assume that initially all particles have equal weight, thus $w_m^b = 1/M$ for $m = 1, \ldots, M$, and that the likelihood is Gaussian with error covariance matrix $\mathbf{R}$, then from (2.3) w_m^a is given by

$$w_m^a = \frac{\exp\left[-\frac{1}{2}(\mathbf{H}\mathbf{z}_m^b - \mathbf{y}_{\text{obs}})^T \mathbf{R}^{-1} (\mathbf{H}\mathbf{z}_m^b - \mathbf{y}_{\text{obs}})\right]}{\sum_{j=1}^{M} \exp\left[-\frac{1}{2}(\mathbf{H}\mathbf{z}_j^b - \mathbf{y}_{\text{obs}})^T \mathbf{R}^{-1} (\mathbf{H}\mathbf{z}_j^b - \mathbf{y}_{\text{obs}})\right]}, \quad m = 1, \ldots, M. \tag{2.7}$$

We look for an optimal coupling matrix $\mathbf{T}^*$ with elements t_{mj}^* which minimizes the squared Euclidean distance and is characterized by a linear programming problem [29] as shown below

$$J(t_{mj}) = \sum_{m,j=1}^{M} t_{mj} ||\mathbf{z}_m^b - \mathbf{z}_j^b||^2.$$

Once we have the optimal coupling matrix $\mathbf{T}^*$ the analysis ensemble members are then calculated by the following linear transformation

$$\mathbf{z}_j^a = M \sum_{m=1}^{M} t_{mj}^* \mathbf{z}_m^b, \quad j = 1, \ldots, M. \tag{2.8}$$

We use $FastEMD$ algorithm developed by Pele & Werman [24] to solve the linear transport problem and get the optimal transport matrix.

***Remark*:** An important property of EnTPF is to retain the imposed interval bounds of ensemble members. Consider an ensemble of background states $\{\mathbf{z}_m^b\}_{m=1}^M$ given by

$$\mathbf{z}_m^b = \begin{bmatrix} a_m^b & b_m^b & c_m^b \end{bmatrix}^T, \quad m = 1, \ldots, M,$$

where we assume all the parameters $\{a_m^b\}_{m=1}^M$, $\{b_m^b\}_{m=1}^M$ and $\{c_m^b\}_{m=1}^M$ are bounded between 0 and 1. Therefore, the following inequalities hold:

$$\begin{cases} 0 < a_{min} \leq a_m^b \leq a_{max} < 1, & m = 1, \ldots, M, \\ 0 < b_{min} \leq b_m^b \leq b_{max} < 1, & m = 1, \ldots, M, \\ 0 < c_{min} \leq c_m^b \leq c_{max} < 1, & m = 1, \ldots, M. \end{cases}$$

Now we assume two discrete random variables B_1 and B_2 have probability distributions given by

$$\pi(B_1 = \mathbf{z}_m^b) = 1/M, \quad \pi(B_2 = \mathbf{z}_m^b) = w_m^a,$$

with $w_m^a \geq 0$, $m = 1, \ldots, M$ and $\sum_{m=1}^{M} w_m^a = 1$. As, EnTPF looks for a matrix $\mathbf{T}^*$

which defines coupling between these two probability distributions, each entry of this coupling matrix satisfies the conditions given by equations (2.4)–(2.6). These conditions assure that each entry of the coupling matrix will be non-negative and less than 1.

Therefore, since the analysis given by (2.8) is

$$\mathbf{z}_m^a = \begin{bmatrix} a_1^b(Mt_{1m}^*) + a_2^b(Mt_{2m}^*) + \cdots + a_M^b(Mt_{Mm}^*) \\ b_1^b(Mt_{1m}^*) + b_2^b(Mt_{2m}^*) + \cdots + b_M^b(Mt_{Mm}^*) \\ c_1^b(Mt_{1m}^*) + c_2^b(Mt_{2m}^*) + \cdots + c_M^b(Mt_{Mm}^*) \end{bmatrix}, \quad m = 1, \ldots, M,$$

these conditions lead to

$$\begin{cases} 0 < a_{min} \leq a_m^a \leq a_{max} < 1, & m = 1, \ldots, M, \\ 0 < b_{min} \leq b_m^a \leq b_{max} < 1, & m = 1, \ldots, M, \\ 0 < c_{min} \leq c_m^a \leq c_{max} < 1, & m = 1, \ldots, M. \end{cases}$$

Thus the coupling matrix bounds the analysis ensemble members to be in the desired range. This is not observed in EnSRF as the matrix $\mathbf{S}$ given by (2.2) does not impose any of the non-equality and equality constraints (see expressions (2.4)–(2.5)), so it results in values outside the bound as well.

2.3 Limitations of EnSRF and EnTPF algorithms

All variations of ensemble Kalman filter and particle filter are limited by the ensemble size. Since, even if the size of the model state is just upto a few thousands, a large ensemble size will make each run of the model computationally very expensive. This limit of small ensemble size to evaluate model statistics introduces sampling error. To deal with the issue of small ensemble size researchers have introduced techniques like *localization* and *ensemble inflation*.

Localization reduces the impact of spurious correlations due to small ensemble size. We will use a distance based localization method, according to which all the observations outside a certain radius around the grid point in concern do not have any effect on the update of the state at that grid point. Since EnSRF updates anomalies in the linear space of ensemble instead of model space we implement the "local analysis" localization method by updating the transformation matrix $\mathbf{S}$ [13]. For the local update of ith element of an ensemble member depending on the grid point i, we first introduce the diagonal matrix $\hat{\mathbf{C}}_i \in R^{N_y \times N_y}$ in observation space which depends on the distance between the updated element and the observation, as defined by,

$$(\hat{\mathbf{C}}_i)_{ll} = \rho\left(\frac{|X_i - r_l|_L}{r_{loc}}\right), \tag{2.9}$$

where $i = 1, \ldots, n^2$, $l = 1, \ldots, N_y$, n^2 is the dimension of the model space, N_y is the dimension of the observation space, r_l denotes the location of the observation, r_{loc} is the *localisation radius* and $\rho(\cdot)$ is a taper function, such as Gaspari-Cohn function [8]

$$\rho(s) = \begin{cases} 1 - \frac{5}{3}s^2 + \frac{5}{8}s^3 + \frac{1}{2}s^4 - \frac{1}{4}s^5, & 0 \leq s \leq 1, \\ -\frac{2}{3}s^{-1} + 4 - 5s + \frac{5}{3}s^2 + \frac{5}{8}s^3 - \frac{1}{2}s^4 + \frac{1}{12}s^5, & 1 \leq s \leq 2, \\ 0, & 2 \leq s. \end{cases}$$

Now to implement this in the algorithm we need to define ensemble anomalies at each grid point X_i

$$\mathbf{A}^b(X_i) = \left[(\mathbf{z}_1^b(X_i) - \bar{\mathbf{z}}^b(X_i)) \quad (\mathbf{z}_2^b(X)_i - \bar{\mathbf{z}}^b(X_i)) \quad \ldots \quad (\mathbf{z}_M^b(X_i) - \bar{\mathbf{z}}^b(X_i))\right],$$

and using this we can define local analysis ensemble anomalies as $\mathbf{A}^a(X_i) := \mathbf{A}^b(X_i)\mathbf{S}(X_i)$. The localised transformation matrix is then given by:

$$\mathbf{S}(X_i) = \left[\mathbf{I} + \frac{1}{M-1}(\mathbf{H}\mathbf{A}^b)^T(\hat{\mathbf{C}}_i\mathbf{R}^{-1})\mathbf{H}\mathbf{A}^b\right]^{-1/2}.$$

For EnTPF we localize the impact of observations by modifying the likelihood of $\mathbf{z}_m^b$ given observation $\mathbf{y}_{\text{obs}}$. Thus (2.7) becomes

$$w_m^a(X_i) = \frac{\exp\left[-\frac{1}{2}(\mathbf{H}\mathbf{z}_m^b - \mathbf{y}_{\text{obs}})^T(\hat{\mathbf{C}}_i\mathbf{R}^{-1})(\mathbf{H}\mathbf{z}_m^b - \mathbf{y}_{\text{obs}})\right]}{\sum_{j=1}^M \exp\left[-\frac{1}{2}(\mathbf{H}\mathbf{z}_j^b - \mathbf{y}_{\text{obs}})^T(\hat{\mathbf{C}}_i\mathbf{R}^{-1})(\mathbf{H}\mathbf{z}_j^b - \mathbf{y}_{\text{obs}})\right]}, \quad m = 1, \ldots, M,$$

where $\hat{\mathbf{C}}_i$ is a diagonal matrix as defined by (2.9). $w_m^a(X_i)$ describes the weight of mth ensemble member of analysis at ith grid point X_i. Moreover, for finding the optimal coupling matrix $\mathbf{T}^*$ we define the associated distance at each grid point by

$$||\mathbf{z}_m^b - \mathbf{z}_j^b||_i^2 = [z_m^b(X_i) - z_j^b(X_i)]^2, \quad m, j = 1, \ldots, M,$$

which reduces the localized EnTPF to a univariate transport problem [26].

In addition to localization, inflation is often used to compensate for a small ensemble. Inflation increases ensemble spread about its mean in order to avoid underestimation of system error covariance, as it can lead to the divergence of the filter. For EnSRF we implement multiplicative inflation [2], where inflated ensemble members are defined as,

$$\mathbf{z}_m^b = \bar{\mathbf{z}}^b + \alpha \mathbf{A}_m^b, \quad m = 1, \ldots, M.$$

Here $\bar{\mathbf{z}}^b$ is background empirical mean, $\mathbf{A}_m^b$ represents background ensemble anomalies and α is the inflation factor (usually $1 < \alpha < 1.2$).

EnTPF can lead to creation of identical or near-identical analysis ensemble members, thus we implement additive inflation [12] to avoid filter divergence and the creation of identical analysis ensemble members by modifying (2.8) to:

$$\mathbf{z}_j^a = M \sum_{m=1}^{M} t_{mj}^* \mathbf{z}_m^b + \epsilon_j, \quad j = 1, \ldots, M, \tag{2.10}$$

where $\{\epsilon_j\}_{j=1}^M$ are independent realizations of random variables from Gaussian distribution $\mathcal{N}(0, \tau C^b)$, $\tau > 0$ here is the rejuvenation factor and it relates to inflation factor by $\alpha = \sqrt{1+\tau^2}$ [4]. For our numerical experiments we use a value of τ ranging from 0 (denoting no rejuvenation) to 0.4, this gives us a range of α from 1 to 1.07. In the rest of the paper we will refer both τ and α as *inflation factor*, and both multiplicative and additive inflation as *inflation*.

For parameter estimation, the quality of the initial guess about the uncertain model parameters influences the ability of data assimilation methods to obtain an accurate estimation of those parameters. If we do not have adequate knowledge about it then the available data may not be enough to improve a poor initial guess. In such cases, it has been found useful to iterate the filter globally as it provides a new and improved initial guess which is closer to the true solution to restart the procedure [16]. There exist several approaches for iterative Kalman filters though that is not the case for EnTPF. Therefore, in this article we use the iterative approach for both EnSRF and EnTPF. Hence, the algorithm runs as follows. We start with an initial guess of parameters $\{\mathbf{u}_m^b\}_{m=1}^M$ and solve the forward model to evaluate the corresponding state $\{\mathbf{P}_m^b\}_{m=1}^M$. This gives us a background ensemble $\{\mathbf{z}_m^b\}_{m=1}^M$ for the first iteration. Then using a data assimilation method with *all the observations* we obtain an analysis $\{\mathbf{z}_m^a\}_{m=1}^M$ at the end of the first iteration of the data assimilation cycle. Since the updated values of the state are conditioned on the observations we expect $\{\mathbf{u}_m^a\}_{m=1}^M$ to be closer to the true value of parameter as compared to $\{\mathbf{u}_m^b\}_{m=1}^M$, therefore $\{\mathbf{u}_m^a\}_{m=1}^M$ are used in the forward problem to generate a new background state for the next iteration. The next iteration is done by rerunning a data assimilation method based on the *same set of observations*. This procedure is usually repeated until we meet any of the imposed stopping criteria. Though we have knowledge regarding these stopping criteria for ensemble Kalman filter from earlier research works, e.g. [14], there is still no literature available regarding it for EnTPF. Hence, to have a fair comparison of these two methods we run the simulations for a fixed number of iterations to study the behavior of the resulting error with number of iterations.

3 Numerical approximation of forward model

We consider a steady-state single-phase Darcy flow model defined over an aquifer of two-dimensional physical domain $D = [0, 1] \times [0, 1]$, which is given by,

$$-\nabla \cdot (k(x, y) \nabla P(x, y)) = f(x, y), \quad (x, y) \in D \tag{3.1}$$

$$P(x, y) = 0, \quad (x, y) \in \partial D \tag{3.2}$$

where $\nabla = \begin{bmatrix} \partial/\partial x & \partial/\partial y \end{bmatrix}^T$, T denotes the transpose, $\cdot$ the dot product, $P(x, y)$ the pressure, $k(x, y)$ the permeability, $f(x, y)$ the source term, which we assume to be $2\pi^2 \sin(\pi x) \sin(\pi y)$, and ∂D the boundary

of domain D. The forward problem of this second order elliptical equation is to find the solution of pressure $P(x, y)$ for given $f(x, y)$ and $k(x, y)$.

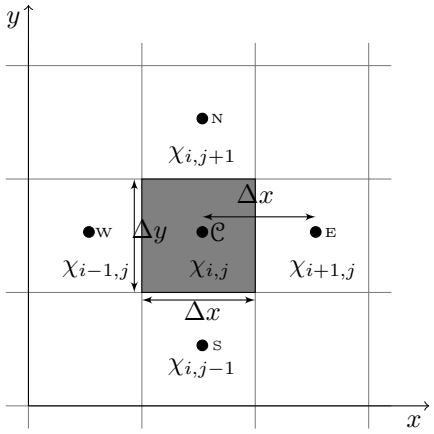

Fig. 1: Grid point cluster

We implement cell-centered finite difference method to discretize the partial differential equation by employing the grid point cluster shown in figure 1, see e.g. [23]. We divide the entire domain D uniformly ($\Delta x = \Delta y$) in $n \times n$ axis-parallel cells of size Δx^2. Each of these cells is denoted by $\chi_{i,j}$, $i, j = 1, \ldots, n$, and has a value of pressure $P_{i,j}$ at its center. For the shaded cell $\chi_{i,j}$ as shown in Figure 1, the grid point $\mathcal{C}$ is the interior point as it is surrounded by cells $\chi_{i+1,j}$, $\chi_{i-1,j}$, $\chi_{i,j+1}$ and $\chi_{i,j-1}$ in all directions. For $\mathcal{C}$ the grid point in its east side, E, has a value of pressure $P_{i+1,j}$, the grid point W in west side has a value of pressure $P_{i-1,j}$, the grid point N on the north side has a value of pressure $P_{i,j+1}$ and the grid point S in south has a value of pressure $P_{i,j-1}$. Integrating (3.1) by parts for cell $\chi_{i,j}$ and replacing the normal derivative on the edges by

$$\left(\frac{\partial P}{\partial x}\right)_{\mathcal{C},E} = \frac{P_{i+1,j} - P_{i,j}}{\Delta x}, \quad \left(\frac{\partial P}{\partial x}\right)_{\mathcal{C},W} = \frac{P_{i,j} - P_{i-1,j}}{\Delta x},$$

$$\left(\frac{\partial P}{\partial y}\right)_{\mathcal{C},N} = \frac{P_{i,j+1} - P_{i,j}}{\Delta y}, \quad \left(\frac{\partial P}{\partial y}\right)_{\mathcal{C},S} = \frac{P_{i,j} - P_{i,j-1}}{\Delta y},$$

gives the finite difference equation for the interior points as

$$-k_{i-1/2,j}(P_{i-1,j} - P_{i,j}) - k_{i+1/2,j}(P_{i+1,j} - P_{i,j}) - k_{i,j-1/2}(P_{i,j-1} - P_{i,j}) - k_{i,j+1/2}(P_{i,j+1} - P_{i,j}) = f_{i,j}\Delta x^2. \tag{3.3}$$

Here $k_{i-1/2,j} = k(x_{i-1/2}, y_j)$ is the value of permeability on the edge between grid points W and $\mathcal{C}$. If k is discontinuous along the interface we take $k_{i-1/2,j}$ as the harmonic mean of the neighboring grid points as

$$k_{i-1/2,j} = \frac{2k_{i-1,j}k_{i,j}}{k_{i-1,j} - k_{i,j}}, \tag{3.4}$$

and similarly $k_{i+1/2,j}$, $k_{i,j-1/2}$ and $k_{i,j+1/2}$ are defined. We implement the Dirichlet boundary conditions (3.2) with the discretized equation (3.3) to derive finite difference equations for the grid points near boundaries, and finally end up with a set of linear equations of the form

$$\mathcal{K}\mathbf{P} = \mathbf{F}, \tag{3.5}$$

where $\mathcal{K}$ is a sparse, symmetric, positive definite matrix of size $n^2 \times n^2$, $\mathbf{P}$ is a vector with entries of P_i, $i = 1, \ldots, n^2$ and $\mathbf{F}$ is a vector with entries f_i for $i = 1, \ldots, n^2$.

4 Numerical Experiments

We perform numerical experiments with synthetic observations, where instead of a measuring device a model is used to obtain observations. We implement cell-centered finite difference method to discretize the

domain D into 100×100 grid cells and solve the forward model given by (3.5) with the *true* parameters. Then the synthetic observations are obtained by

$$\mathbf{y}_{\text{obs}} = \mathbf{L}(\mathbf{P}) + \eta, \tag{4.1}$$

where an element of $\mathbf{L}(\mathbf{P})$ is a linear functional of pressure, namely

$$L_l(\mathbf{P}) = \frac{1}{2\pi\sigma^2} \sum_{i=1}^{n^2} \exp\left(-\frac{|X_i - r_l|^2}{2\sigma^2}\right) P_i \Delta x^2, \quad l \in 1, \ldots, N_y \tag{4.2}$$

where $\sigma = 0.01$ and $N_y = 16$ represents the number of observation locations. The observation locations are spread uniformly across the domain D as shown by the dots in figure 3 and 9. η denotes the observation noise and is assumed to be a random variable drawn from a normal distribution with mean zero and standard deviation of 0.09. It is important to note that for the inverse problem we use grid size of 50×50 to make the problem in hand more challenging.

4.1 Low-dimensional test case

For our first numerical experiment, we consider a low-dimensional problem where the permeability field is defined by mere 5 parameters. We assume that the entire domain $D = [0, 1] \times [0, 1]$ is divided into two subdomains D_1 and D_2 as shown in figure 2. Each subdomain of D represents a layer and is assumed to have a permeability function $k(\mathbf{X})$, where an element of $\mathbf{X}$ is defined by $X_i = \chi_{g,j}$, for $i = 1, \ldots, n^2$ and $g, j = 1, \ldots, n$. The thickness of layer on both sides a and b, correspondingly, defines the slope of the interface and a parameter c defines a vertical fault. The layer moves up or down depending on $c < 0$ or $c > 0$, respectively, and its location is assumed to be fixed at $x = 0.5$.

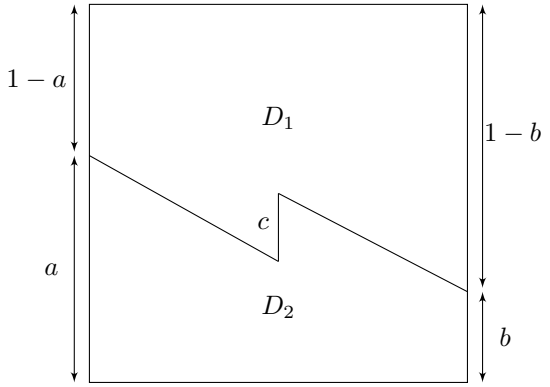

Fig. 2: Geometrical configuration: low-dimensional test case

Further, for this test case we assume piecewise constant permeability within each of the subdomains, hence $k(\mathbf{X})$ is given by

$$k(\mathbf{X}) = k_1 \delta_{D_1}(\mathbf{X}) + k_2 \delta_{D_2}(\mathbf{X}), \tag{4.3}$$

where k_1, k_2 represent permeability of the subdomain D_1, D_2, respectively, and δ is Dirac function. Then the parameters defining the permeability field for this configuration are

$$\mathbf{u} = \begin{bmatrix} a & b & c & k_1 & k_2 \end{bmatrix}^T.$$

We assume the true value of the parameters which defines the geometry to be $a^{true} = 0.6$, $b^{true} = 0.3$, $c^{true} = -0.15$ and that of parameters defining the permeability in different layers as $k_1^{true} = 12$ and $k_2^{true} = 5$. These parameter values are used to create the synthetic observations. Next, we assume all the five uncertain parameters are drawn from a uniform distribution over a specified interval, namely $a, b \sim \mathcal{U}[0, 1]$, $c \sim \mathcal{U}[-0.5, 0.5]$, $k_1 \sim \mathcal{U}[10, 15]$ and $k_2 \sim \mathcal{U}[4, 7]$. Top row of figure 3 shows the true state of permeability based on the true values of parameters with the dots representing the observation locations. Bottom row of the figure illustrates some of the permeability fields defined by different ensemble members providing an impression of the prior state.

As it was pointed out earlier in section 2.2, EnTPF takes into account the physical constraints on the model parameters. However, the particle rejuvenation as given in (2.10) is essential for EnTPF, but

increases the spread among ensemble members without considering these physical constraints. Therefore, we need to change the variables to make sure the output of data assimilation algorithm remains physically viable. As the domain D is $[0,1] \times [0,1]$, the parameters a and b should lie within the interval $[0,1]$. To enforce this constraint we substitute a according to:

$$a' = \log\left(\frac{a}{1-a}\right), \quad a' \in R$$

and similarly b is substituted by b'. The parameter c, however, remains unchanged since we do not have any constraint for it. Further, since permeability should only take non-negative values, we change the parameter k to $k' = \log(k)$. Thus the parameters are now given by $\mathbf{u}' = \begin{bmatrix} a' & b' & c & k_1' & k_2' \end{bmatrix}^T$. The state vector $\mathbf{P}$ is then augmented with $\mathbf{u}'$ instead of $\mathbf{u}$, which we later transform back to the parameter $\mathbf{u}$. This change of variables is performed for both EnTPF and EnSRF.

In order to avoid any bias due to initial ensemble we perform 10 simulations based on a random draw of initial ensemble from the same prior distribution. Then to compare the performance of EnTPF and EnSRF, we run a simulation for a maximum of 100 iterations and calculate the root mean squared error (RMSE) at each iteration as:

$$\mathrm{RMSE}(a^r) = \sqrt{\frac{1}{M}\sum_{m=1}^{M}(a_m^{a,r} - a^{true})^2}, \quad r = 1, \ldots, 10,$$

where M is ensemble size and r is the simulation number. We similarly evaluate RMSE for b, c, k_1 and k_2 and use it to calculate the relative RMSE (RE) by

$$\mathrm{RE}^r = \frac{1}{5}\left(\frac{\mathrm{RMSE}(a^r)}{a^{truth}} + \frac{\mathrm{RMSE}(b^r)}{b^{truth}} + \frac{\mathrm{RMSE}(c^r)}{c^{truth}} + \frac{\mathrm{RMSE}(k_1^r)}{k_1^{truth}} + \frac{\mathrm{RMSE}(k_2^r)}{k_2^{truth}}\right), \quad r = 1, \ldots, 10. \quad (4.4)$$

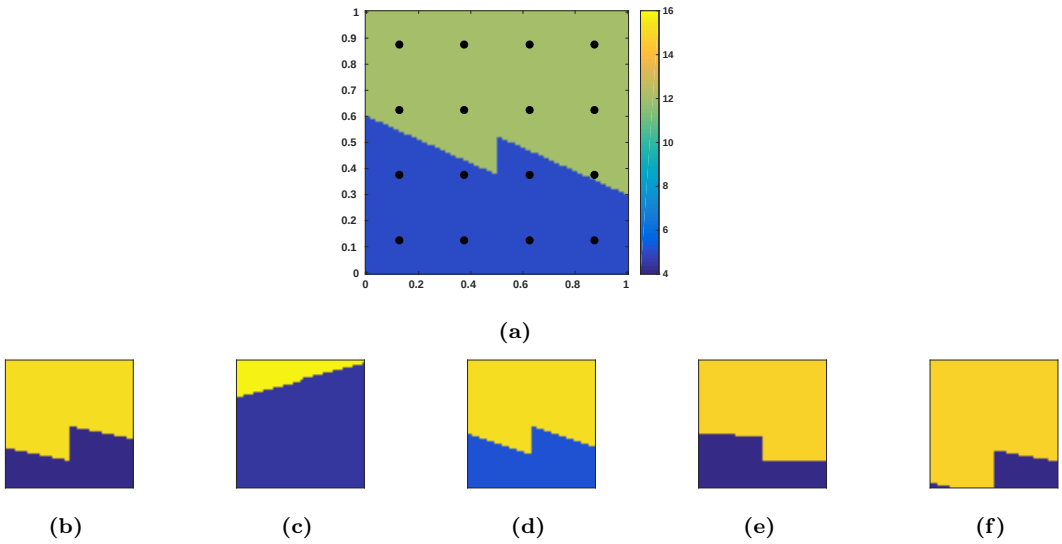

Fig. 3: Permeabilities of low-dimensional test case. Top: truth with dots representing the observation locations. Bottom: permeabilities defined by (4.3) from some samples of the prior.

We conduct the numerical experiments for ensemble sizes varying from 10 to 300 with an increment of 20 and an inflation $\alpha \in [1, 1.077]$ for EnSRF which corresponds to $\tau \in [0, 0.4]$ for EnTPF.

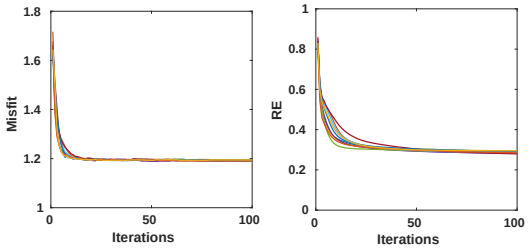

(a) Left: data misfit, right: RE. $\alpha = 1$

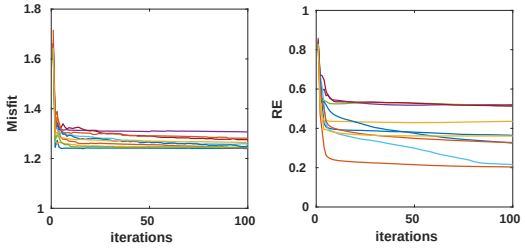

(b) Left: data misfit, right: RE. $\tau = 0$

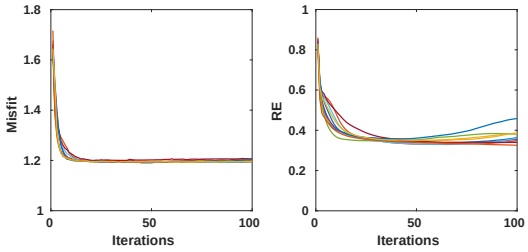

(c) Left: data misfit, right: RE. $\alpha = 1.0284$

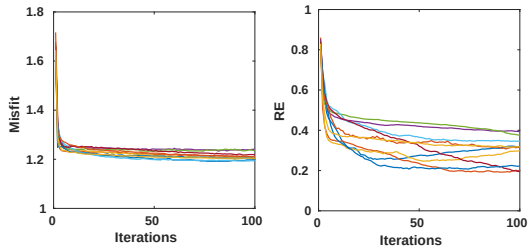

(d) Left: data misfit, right: RE. $\tau = 0.24$

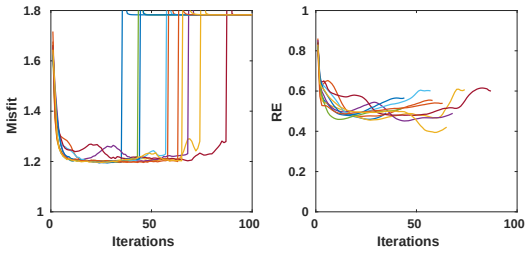

(e) Left: data misfit, right: RE. $\alpha = 1.077$

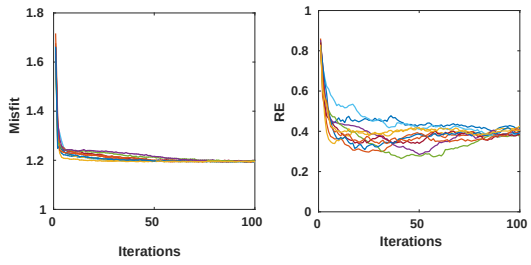

(f) Left: data misfit, right: RE. $\tau = 0.4$

Fig. 4: RE over iterations for M=150 and different inflation factors for EnSRF (a, c, e) and EnTPF (b, d, f) with different colors corresponding to the behavior of different experiments.

Figure 4 represents the variation of RE and data misfit $||\mathbf{y}_{\text{obs}} - \mathbf{L}(\mathbf{P})||$, where $||\cdot||$ denotes L^2 norm, for each of the 10 simulations with respect to iterations at an ensemble size of 150 and inflation factor varying from the smallest we use α=1 (τ=0) to the highest α=1.077 (τ=0.4) for EnSRF (EnTPF). Here same color lines represent the behavior of the same set of initial ensemble for both the data misfit plot and the corresponding RE plot. We observe that at α=1 for EnSRF the data misfit and RE behave similarly and converge to a minimum value, which moreover is nearly same for all the 10 simulations as shown in figure 4(a). Thus, at low inflation factors EnSRF is independent of initial ensemble. At $\alpha \geq 1.0284$ even though data misfit attains convergence the corresponding RE for some simulations starts increasing with iterations as shown in figure 4(c). This is a well known fact and to avoid such occurrence different regularization methods are applied to stop iterations before this trend begins. Any further increment in α leads to more disastrous results for EnSRF as shown in figure 4(e). Therefore, since we observe discrepancy between the behavior of data misfit and RE for M=150 at $\alpha \geq 1.0284$, we study the effect of inflation in terms of ensemble size. In figure 5 we plot MRE over 10 simulations as

defined by:

$$\text{MRE} = \frac{1}{10}\sum_{r=1}^{10} \text{RE}^r, \tag{4.5}$$

as a function of ensemble size. In black line with circular markers we plot MRE at the last iteration at no inflation, and in black line with star markers MRE at last iteration at optimal inflation (when MRE is the lowest). It can be observed from this figure that for EnSRF inflation does not seem to improve the results if we compare the MRE at the last iteration. However, if we compare the lowest MRE over iterations at optimal inflation and no inflation as shown in figure 5 using red line with diamond markers and red line with triangle markers, respectively, we see an improvement. The MRE is smaller due to inflation but only at the lowest ensemble size M=10, and as the ensemble size increases α=1 (which corresponds to no inflation) becomes the optimal inflation factor. Therefore, the behavior shown in figure 4 (c) and (e) can be credited to large inflation which should be avoided. It should also be noted that for ensemble size greater than 10 and no inflation the MRE at the last iteration is the same as the lowest MRE over iterations.

In figure 4 (b, d, f) we show the RE with respect to the number of iterations for EnTPF at M=150 and $\tau \in [0, 0.4]$, where each curve represents the behavior of different initial ensemble. As it can be seen from figure 4 (b) unlike EnSRF here behavior of each simulation differs from another at low values of $\tau \in [0, 0.24]$, with each attaining a different minimum value of data misfit and especially RE. As we increase the inflation factor $\tau > 0.24$ we observe convergence among all the simulations and at $\tau = 0.4$ the data misfit as well as the RE attains maximum convergence (shown in figure 4 (f)). In figure 5 (b) we show the MRE as a function of ensemble size for EnTPF. We plot the MRE at the last iteration at no inflation and at optimal inflation in black without any markers and in black with square markers, respectively. In red we plot the lowest MRE over iterations, where no markers refer to no inflation and square markers to optimal inflation. It can be observed from the figure that unlike EnSRF EnTPF performance improves with inflation, as EnTPF creates nearly identical ensemble members which remain the same in a deterministic system unless inflation is applied. Also, for EnTPF the lowest MRE over iterations is lower than the MRE at the last iteration for any ensemble size which suggests that implementing stopping criteria might help to improve the results of EnTPF.

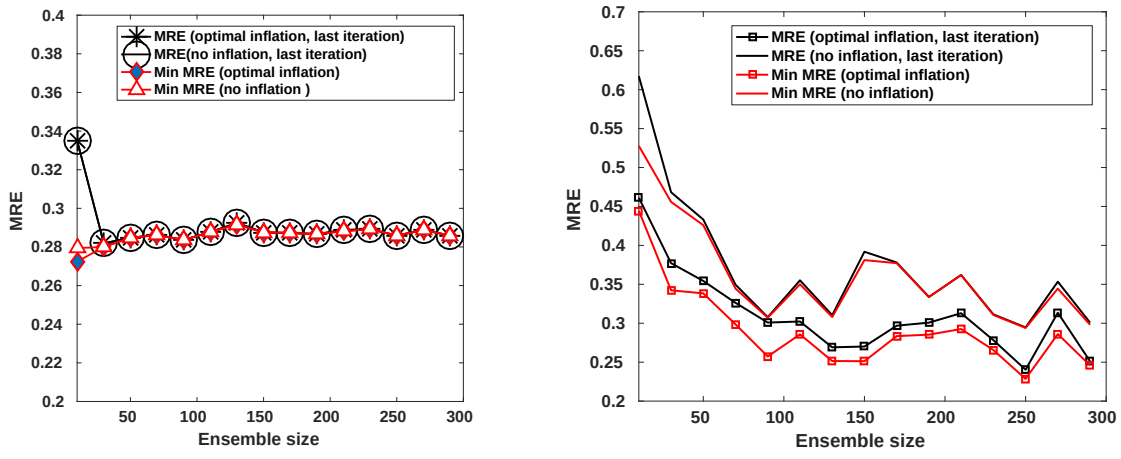

Fig. 5: MRE as a function of ensemble size for EnSRF (a) and EnTPF (b). For EnSRF, black line represents MRE at last iteration with star markers denoting optimal inflation and circular markers no inflation. Red line with diamond markers and triangle markers represent the lowest MRE over iteration at optimal inflation and no inflation, respectively. For EnTPF, black line denotes MRE at last iteration with square markers representing optimal inflation and without markers representing no inflation. Red line with and without markers represents lowest MRE over iteration at optimal and no inflation, respectively.

To have a better idea of the effect of inflation factor and ensemble size on the performance of EnSRF and EnTPF we plot the heatmaps using the lowest MRE over iterations for both data assimilation schemes in figure 6. It can be seen from the heatmap of EnSRF (b) that the results remain almost the same for all ensemble sizes and $\alpha \geq 1.0127$ ($\tau \geq 0.16$). As the inflation factor increases the MRE starts

increasing suggesting divergence of the algorithm. For EnTPF (figure 6 (a)), MRE improves as ensemble size increases and the optimal inflation factor varies with the ensemble size.

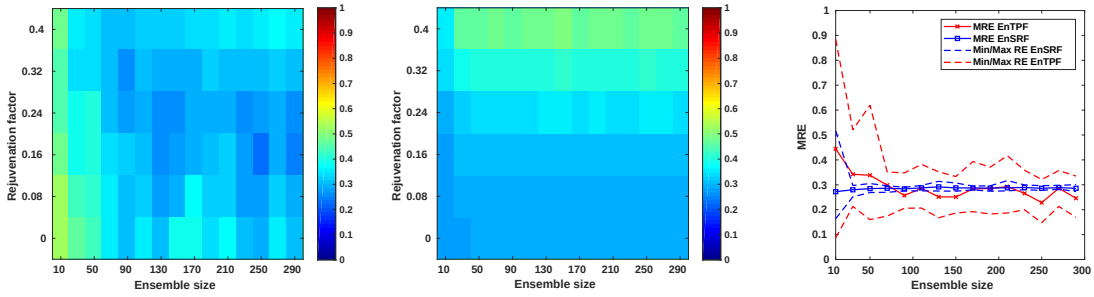

(a) **(b)** **(c)**

Fig. 6: Heatmaps showing the best MRE over iterations for EnTPF (a) and EnSRF (b). Lowest MRE over iteration using optimal inflation factor is shown in solid red for EnTPF and solid blue for EnSRF with dashed lines representing minimum and maximum RE among the 10 simulation corresponding to the lowest MRE (c).

Figure 6 (c) provides a clear comparison in performance between the data assimilation schemes. We plot the lowest relative error over iterations at optimal inflation for EnSRF in blue and for EnTPF in red. The solid lines represents the mean over 10 simulations (4.5) and the dashed line represents the minimum and maximum RE (4.4) over 10 simulations. It can be observed from this figure that EnSRF provides better results than EnTPF at lower ensemble sizes, though as ensemble size increases we can see improvement in the results of EnTPF and at around M=70 it becomes comparable to that of EnSRF. With further increase in the ensemble size ($M \geq 70$) the results of EnTPF either remain the same as EnSRF or become better. It can also be noted that the difference between the maximum RE and minimum RE is large for EnTPF, which signifies the dependence of EnTPF on the choice of initial ensemble. This suggests that the results of EnTPF can be improved if one makes a more educated guess of initial ensemble. For EnSRF on the contrary the difference between the maximum and minimum RE is almost negligible for $M \geq 30$ making the method more robust.

Since the relative error does not provide a clear picture of the estimation of parameters individually, we illustrate them in figure 7. We evaluate the mean and spread of parameters at the end of each iteration, which we average over 10 simulations as:

$$\bar{\bar{a}}^a = \frac{1}{10}\sum_{r=1}^{10} \bar{a}^{a,r},$$

here $\bar{a}^{a,r} = \frac{1}{M}\sum_{m=1}^{M} a_m^{a,r}$ for $r = 1, \ldots, 10$, and $\bar{\bar{a}}^a \pm 1.5\bar{a}^a_{spread}$, where

$$\bar{a}^a_{spread} = \frac{1}{10}\sum_{r=1}^{10}\sqrt{\frac{1}{M}\sum_{m=1}^{M}(a_m^{a,r} - \bar{a}^{a,r})^2},$$

where superscript a stands for analysis, and similarly for b, c, k_1 and k_2.

Figure 7 shows the mean of parameters over ensemble size at the optimal inflation factor and at the iteration which provides the lowest MRE. In this figure, the solid black line represents the true value of parameters, the solid blue line represents the mean parameter values for EnSRF and solid red line for EnTPF. The dashed lines show $\bar{\bar{\mathbf{u}}}^a \pm 1.5\bar{\mathbf{u}}_{spread}$ for EnSRF in blue and EnTPF in red. It can be observed from figure 7 that for EnSRF from $M = 10$ until $M = 50$ the mean value of some of the parameters improves while some others get worse but starting from $M = 50$ they all remain unchanged. On the other hand, for EnTPF they keep fluctuating as ensemble size increases. It is evident from this figure that neither EnTPF nor EnSRF provides consistently with a better estimation of each of the five parameters, as at some ensemble sizes for parameter a and c it is EnTPF that provides with the best results and for parameters b and k_2 it is EnSRF. For k_1, which denotes the high permeability, both these methods fail to provide with a good estimation, as k_1 leads to low pressure values which correspond to very small values of data misfit $||\mathbf{y}_{\text{obs}} - \mathbf{L}(\mathbf{P})||$ and as a result does not provide an effective correction of the ensemble members.

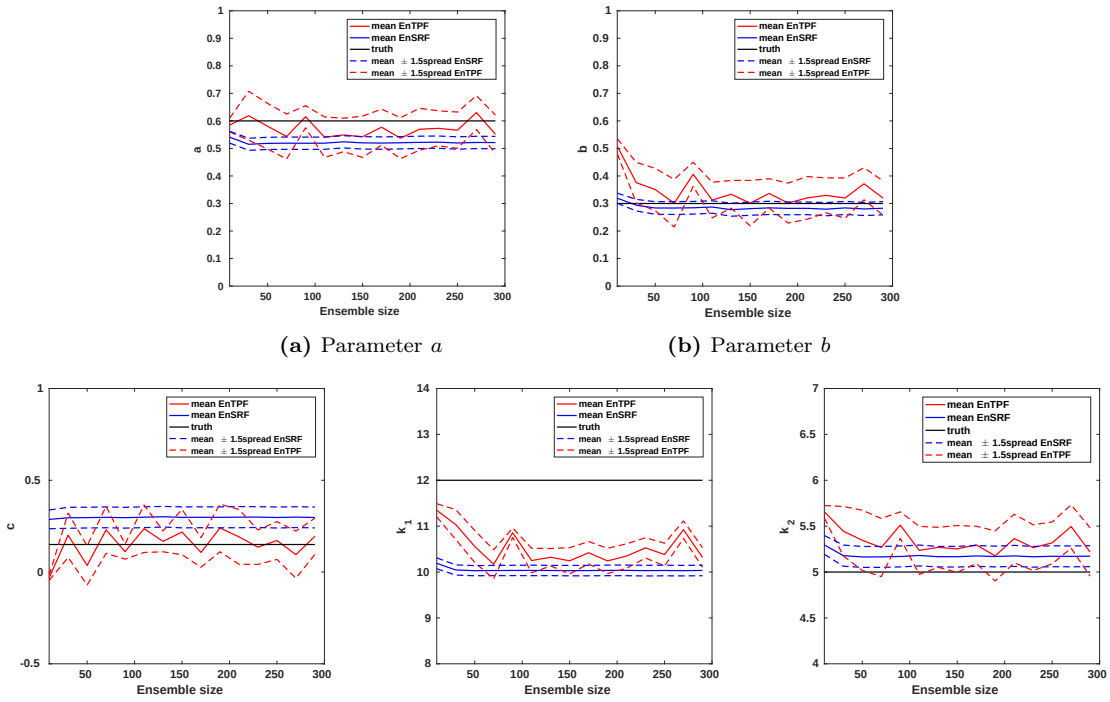

(a) Parameter a **(b)** Parameter b

(c) Parameter c **(d)** Parameter k_1 **(e)** Parameter k_2

Fig. 7: Variation for $\bar{\mathbf{u}}^a$ and $\bar{\mathbf{u}}^a \pm 1.5\bar{\mathbf{u}}_{spread}$ w.r.t ensemble size for at the iteration resulting in least MRE for EnTPF(red) and EnSRF(blue) schemes. Solid black line represents the true value.

4.2 High-dimensional test case

Next, we consider a high-dimensional problem. The domain D is again divided into two subdomains D_1 and D_2 though without a fault as shown in figure 8. The parameters a and b define the thickness of layers. However, unlike in the previous test case here we implement a spatially varying permeability field which is defined at each grid point as:

$$k(\mathbf{X}) = k_1(\mathbf{X})\delta_{D_1}(\mathbf{X}) + k_2(\mathbf{X})\delta_{D_2}(\mathbf{X}). \tag{4.6}$$

Hence, the parameters defining the permeability field for this configuration are:

$$\mathbf{u} = \begin{bmatrix} k(X_1) & k(X_2) & \dots & k(X_{n^2}) \end{bmatrix}^T,$$

where n^2 is the grid size. Since permeability should only take non-negative values, we change the parameter k to $k' = \log(k)$. Thus the parameters for this test case are given by $\mathbf{u}' = k'(\mathbf{X})$ where $k'(\mathbf{X}) = \log(k(\mathbf{X}))$. The state vector is then augmented with $\mathbf{u}'$ instead of $\mathbf{u}$, which we later transform back to the parameter state $\mathbf{u}$.

We assume the permeability in the subdomains D_1 and D_2 are generated by random draws from Gaussian distributions $\mathcal{N}(\mathbf{1}, \boldsymbol{C}_1)$ and $\mathcal{N}(\mathbf{5}, \boldsymbol{C}_2)$, respectively. Here $\mathbf{1}$ is a n^2 vectors represented by $\mathbf{1} = \begin{bmatrix} 1 & 1 & \dots & 1 \end{bmatrix}^T$, $\mathbf{5}$ is a n^2 vectors represented by $\mathbf{5} = \begin{bmatrix} 5 & 5 & \dots & 5 \end{bmatrix}^T$, $\boldsymbol{C}_1$ is assumed to be a spherical correlation with maximum correlation along $\pi/4$ and $\boldsymbol{C}_2$ to be an exponential correlation with maximum correlation along $3\pi/4$, an element of $\mathbf{C}_1$ and $\mathbf{C}_2$ is shown below using [22]:

$$C_{1i,j} = \begin{cases} 1 - \dfrac{3h_{i,j}}{2v} + \dfrac{h_{i,j}^3}{2v^3}, & 0 \le h_{i,j} \le v, \\ 0, & h_{i,j} \ge v, \end{cases} \tag{4.7}$$

$$C_{2i,j} = \exp(-3(|h_{i,j}|/v)), \tag{4.8}$$

for $i, j = 1, \dots, n^2$. Here $h_{i,j}$ is the distance between two spatial locations and v is the correlation range which is taken to be 0.5.

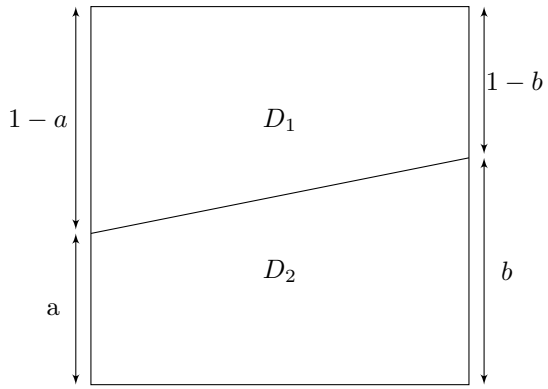

Fig. 8: Geometrical configuration: high-dimensional test case

As the covariance matrices are symmetric (from (4.7) and (4.8)) we factorize them in upper and lower triangular matrices using Cholesky decomposition and represent the upper triangular matrix of $\mathbf{C}_1$ with $\mathbf{G}_1$ and of $\mathbf{C}_2$ with $\mathbf{G}_2$. Next, we generate realizations of a vector $\mathcal{Z}$ with dimension n^2 from a Gaussian distribution with mean zero and variance 1. Using this we create the permeability fields $\mathbf{k}_1'(\mathbf{X})$ with mean $\bar{\mathbf{k}}_1'$ and covariance $\mathbf{C}_1$ and $\mathbf{k}_2'(\mathbf{X})$ with mean $\bar{\mathbf{k}}_2'$ and covariance $\mathbf{C}_2$ across the entire domain D as follows:

$$\begin{cases} \mathbf{k}_1' = \bar{\mathbf{k}}_1' + \mathbf{G}_1^T \mathcal{Z}, \\ \mathbf{k}_2' = \bar{\mathbf{k}}_2' + \mathbf{G}_2^T \mathcal{Z}, \end{cases} \tag{4.9}$$

where $\bar{\mathbf{k}}_1'$ and $\bar{\mathbf{k}}_2'$ are vectors of dimension n^2 represented by $\bar{\mathbf{k}}_1' = \begin{bmatrix} \log(1) & \log(1) & \dots & \log(1) \end{bmatrix}^T$ and $\bar{\mathbf{k}}_2' = \begin{bmatrix} \log(5) & \log(5) & \dots & \log(5) \end{bmatrix}^T$, respectively. The parameter $\mathbf{u}'$ is defined at each grid point by

$$\begin{cases} \mathbf{u}_i' = \mathbf{k}_{1i}', & X_i \in D_1, \\ \mathbf{u}_i' = \mathbf{k}_{2i}', & X_i \in D_2. \end{cases} \tag{4.10}$$

For synthetic observation we use the grid size of 100×100, true intercept $a^{true} = 0.11$ and $b^{true} = 0.86$. Then we solve the forward problem (3.5) for $\mathbf{exp}(\mathbf{u}^{true'})$ according to (4.10) and create the noisy observations of pressure by (4.1). The true permeability field of the system is shown in the top row of figure 9 with dots representing the observation locations. For generating the prior we assume the domain is divided into subdomains D_1 and D_2 using samples a, $b \sim \mathcal{U}[0,1]$ and grid size of 50×50, then $\mathbf{u}'$ is defined according to (4.10) and (4.9) but with different realizations of $\mathcal{Z}$. Thus the dimension of the uncertain parameters is 2500. The bottom row of figure 9 shows some of the prior states.

We perform 10 different simulations based on a random draw of initial ensemble from the same prior distribution, as in the previous test case. To compare the performance of EnTPF and EnSRF, we calculate the root mean squared error (RMSE) at each iteration as:

$$\text{RMSE}^r = \frac{1}{2500} \sum_{j=1}^{2500} \sqrt{\frac{1}{M} \sum_{m=1}^{M} (\{\mathbf{u}_m^{a,r}\}_j - \{\mathbf{u}^{true}\}_j)^2}, \quad r = 1, \dots, 10,$$

where M is the ensemble size and r is the simulation number. We implemented 20 iterations as the maximum allowed iteration limit.

In figure 10 we represent the variation of RMSE and data misfit $||\mathbf{y}_{\text{obs}} - \mathbf{L}(\mathbf{P})||$ for each of the 10 simulations with respect to iterations at an ensemble size of 130 and inflation factor varying from the smallest we use α=1 (τ=0) to the highest α=1.077 (τ=0.4) for EnSRF (EnTPF). It can be seen from figure 10 (a) that unlike the previous test case here stopping criteria is required for EnSRF even at α=1 (no inflation) as the RMSE starts increasing for few simulations after around 3 to 4 iterations. However, for $\alpha < 1.0284$ all the simulations attain convergence within 20 iterations. Figure 10 (b) and (c) show that similar to the low-dimensional test case this numerical experiment encounters divergence for $\alpha \geq 1.0284$, and hence reinforces the claim to avoid large inflation factors for EnSRF.

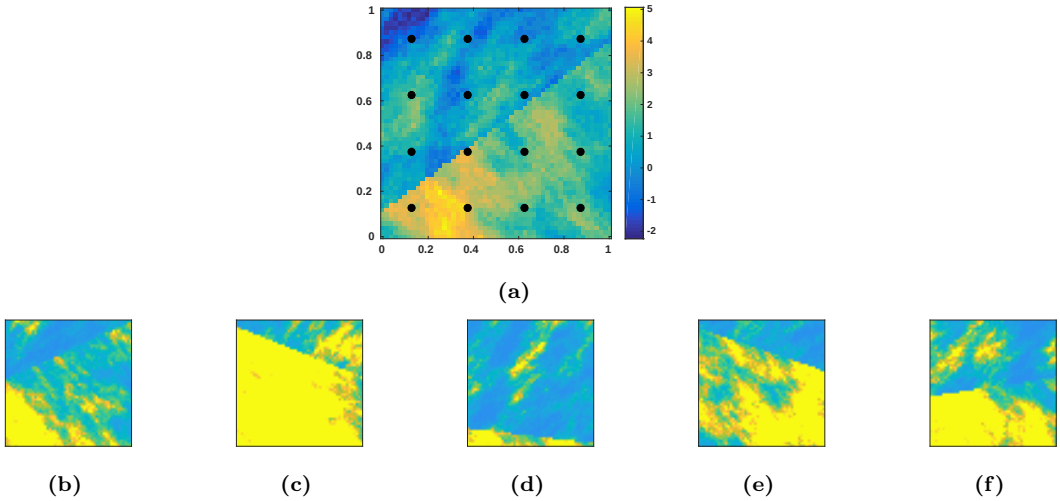

(a) **(b)** **(c)** **(d)** **(e)** **(f)**

Fig. 9: Permeabilities of high-dimensional test case. Top: truth with dots representing the observation locations. Bottom: permeabilities defined by (4.6) from some samples of the prior.

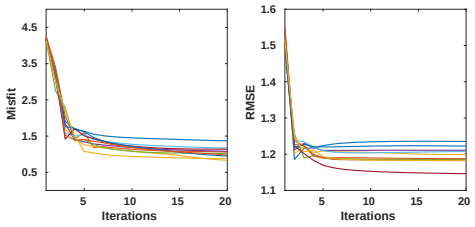

(a) Left: data misfit, right: RMSE. $\alpha = 1.0$

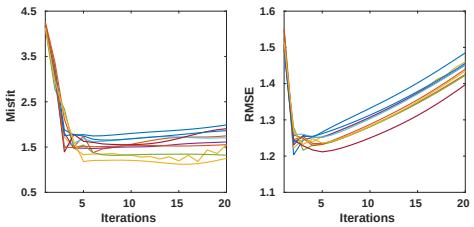

(b) Left: data misfit, right: RMSE. $\alpha = 1.0284$

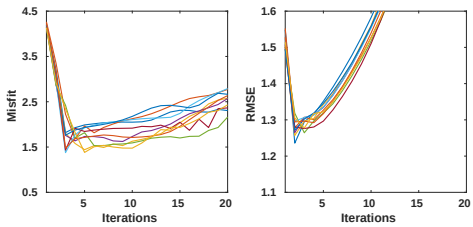

(c) Left: data misfit, right: RMSE. $\alpha = 1.077$

Fig. 10: RMSE and data misfit over iterations for EnSRF with random initial ensemble at M=130 and different inflation factors.

In figure 11 we represent average of RMSE over 10 simulations (MRE) as defined by:

$$\text{MRE} = \frac{1}{10}\sum_{r=1}^{10}\text{RMSE}^r. \tag{4.11}$$

where RMSE is the lowest over iterations. It shows MRE at the optimal inflation factor as a function of ensemble size. MRE for EnSRF using random initial ensemble is represented by solid black line. It should be noted that EnTPF with random initial ensemble results in degenerative weights for at least one of the 10 simulations at each ensemble size and inflation factor implemented, thus not shown in figure 11. This happens because EnTPF depends on the weight defined by the Gaussian likelihood function (2.7) which approaches zero if the initial guess is extremely poor. This suggests that EnTPF is highly dependent on the quality of initial ensemble, as it was observed in the low-dimensional case. Moreover, the issue of degenerative initial weights arises in this test case since we estimate 2500 grid dependent uncertain parameters using small ensemble sizes.

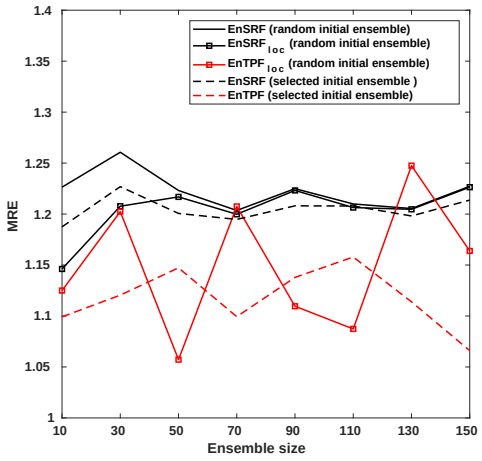

Fig. 11: Best MRE over iterations as a function of ensemble size. EnSRF using random initial ensemble with and without localization in solid black line with and without markers, respectively, and EnTPF using random initial ensemble with localization in solid red line with markers. Dashed line of corresponding color represents MRE of EnTPF and EnSRF using selected initial ensemble.

One of the approaches to overcome the degenerative weights is localization. We implement spatial localization for both EnSRF and EnTPF with radius r_{loc} ranging from 0.2 to 0.8. The inflation factor values are kept the same, i.e. $\tau \in [0, 0.4]$. EnSRF with localization shows similar behavior of the misfit and RMSE as without localization, thus not shown. In figure 11 we show the lowest MRE obtained at a combination of inflation factor and localization radius. It shows the effect of localization using random initial ensemble by solid black line with square markers for EnSRF. As expected, localization provides improved MRE for EnSRF for smaller ensemble sizes. For $M \geq 50$ MRE of EnSRF with localization converges with the MRE of EnSRF without localization, suggesting localization is futile at large ensemble sizes.

For EnTPF the initial degeneracy of weights depends mostly on three factors, namely: extremely low observation error, high number of observations and poor initial guess. Localization solves the problem of degenerative weights locally by reducing the number of observations. Thus we are able to obtain MRE for EnTPF with localization as shown in figure 11 in solid red line with square markers. However, the low observation error and poor initial guess remain unchanged and can still cause divergence from the true solution. As illustrated in figure 11, MRE of EnTPF with localization shows high fluctuation over ensemble sizes with the worst performance at M=130. We represent the RMSE and misfit of each of the 10 simulation for EnTPF with localization at M=130 in figure 12. The undesirable increase of data misfit and RMSE is attributed to the fact that localization converts a global optimization problem to a univariate transport problem which does not always provide the desired global data misfit and RMSE. Moreover, localization does not provide any quality check of the initial ensemble, which impacts the performance of EnTPF as for an extremely poor initial guess localization results in non-zero weights locally but globally the weights remain zero. This suggests that the updated parameters are still away from the truth causing the increase in the misfit and RMSE.

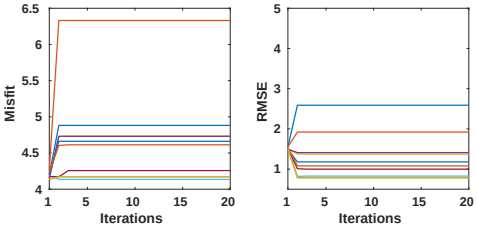

(a) Left: data misfit, right: RMSE. $\tau = 0$

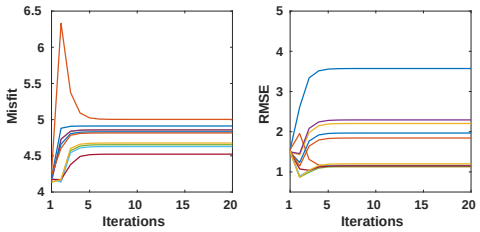

(b) Left: data misfit, right: RMSE. $\tau = 0.24$

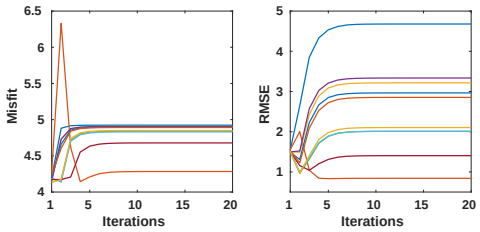

(c) Left: data misfit, right: RMSE. $\tau = 0.4$

Fig. 12: RMSE and data misfit over iterations for EnTPF with random initial ensemble and localization at M=130 and different inflation factors.

Another approach to handle the degenerative weights is by introducing a quality control of an initial ensemble. After a random draw from the prior distribution we compute the analysis weights given by (2.3) and calculate the effective sample size using [26]:

$$M_{\text{eff}} = \frac{1}{\sum_{m=1}^{M} (w_m^a)^2}.$$

If the ensemble members fail to enclose the true state within their range then their respective weights $\{w_m^a\}_{m=1}^M$ approach zero resulting in an undefined value of effective sample size. If we encounter such a situation for any of our initial samples, we redraw a new ensemble and check the value of effective sample size again. Once we have an ensemble which fulfills the above condition then we proceed with the data assimilation iterations and we repeat this process until we have 10 such simulations. Selecting the initial ensemble incurs additional computational cost, as for ensemble size 10 we have to make random draws 100 times, though as ensemble size increases to 50 the rejection rate goes down to 50% and for $M > 70$ it is around 30%.

We illustrate the RMSE and data misfit for numerical experiment with selected initial ensemble without localization for EnTPF in figure 13. We observe that selected initial ensemble provides more stable results than localization. However, at τ=0 some of the simulations start moving away from the true state with iterations (figure 13 (a)). This is due to the creation of identical or near-identical members by EnTPF, which without inflation behave similarly in a deterministic system. The effective sample size for a few simulations dropped to 1 at M=130 without inflation resulting in the increase of misfit and RMSE. For $\tau > 0.08$ we do not observe such behavior (figure 13 (b) and (c)) which further asserts the importance of inflation for EnTPF. As it was expected EnSRF with selected initial ensemble shows similar behavior of the misfit and RMSE as with or without localization (not shown).

In figure 11 the dashed lines show the MRE at optimal inflation factor with selected initial ensemble and without localization. As can be observed from this figure that EnTPF (dashed red line) results in lower MRE than EnSRF for each ensemble size. It is also interesting to note here that for EnSRF the MRE based on an improved guess of initial ensemble are lower than MRE based on random guess of initial ensemble. As ensemble size increases MRE starts converging for all three variations of EnSRF algorithms performed, suggesting its robustness.

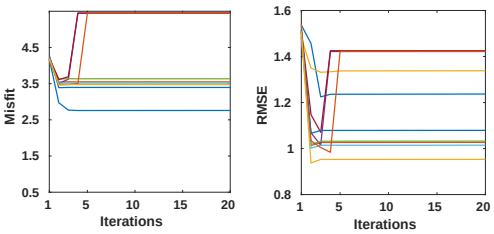

(a) Left: data misfit, right: RMSE. $\tau = 0$

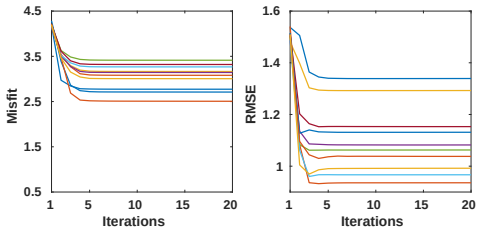

(b) Left: data misfit, right: RMSE. $\tau = 0.24$

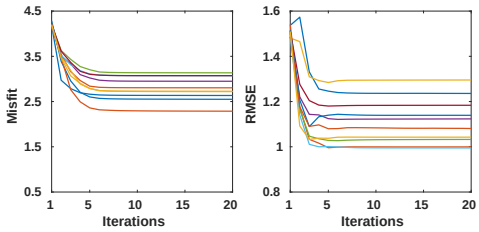

(c) Left: data misfit, right: RMSE. $\tau = 0.4$

Fig. 13: RMSE and data misfit over iterations with selected initial ensemble at M=130 for EnTPF at various inflation factors.

In figure 14 we show heatmaps for EnTPF(a) and EnSRF (b) using selected initial ensemble. EnTPF provides lower MRE than EnSRF at each ensemble size. Moreover, high inflation factors deteriorate the performance of EnSRF as observed in previous test case. Figure 14 (c) provides a clear comparison between EnTPF (red) and EnSRF (blue). In this figure we plot the lowest MRE (solid lines) over iterations along-with the minimum and maximum of lowest RMSE (dashed lines) over iterations among the 10 simulations. It is interesting to note here that for EnSRF at optimal inflation factor the minimum and maximum RMSE values approaches the MRE values as ensemble size increases, while for EnTPF the difference among the minimum and maximum RMSE remains nearly the same at each of the ensemble sizes.

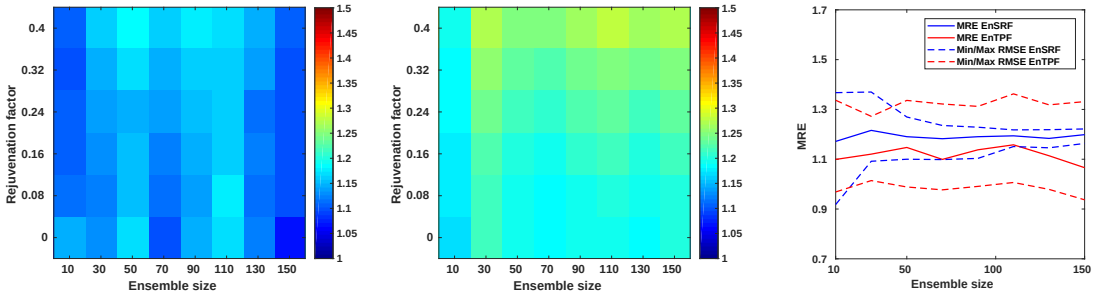

(a) **(b)** **(c)**

Fig. 14: Heatmaps showing the best MRE over iterations for EnTPF (a) and EnSRF (b). Lowest MRE over iteration using optimal inflation factor is shown in solid red for EnTPF and solid blue for EnSRF with dashed lines representing minimum and maximum RMSE among the 10 simulation corresponding to the lowest MRE (c).

5 Conclusions

In this work we investigated the performance of a new data assimilation method for parameter estimation in subsurface flow models. The method is essentially a sequential Monte Carlo approach with a new coupling based resampling technique and is known as ensemble transform particle filter. Important aspects of EnTPF are that it does not make any assumptions of Gaussian distributions and the coupling matrix used for transformation of forecast state to analysis state bounds the ensemble members in a desired range. We tested the performance of EnTPF using the results of ensemble Kalman filter

as a benchmark. The numerical experiments using 2-D Darcy flow model demonstrated that EnTPF provides excellent estimations of permeability fields. Inflation, however, is indispensable for EnTPF for any ensemble size in contrast to EnSRF where inflation is only needed for small ensemble sizes. For small number of parameters (5), EnTPF performs comparably to EnSRF and for large number of parameters (2500) it outperforms the ensemble Kalman filter. However, in order for EnTPF to have non-degenerative weights in the high dimensional test case either localization or quality control has to be implemented. It was observed that localization might results in the RMSE increase over iterations indicating that the updated ensemble is further away from the truth than the initial ensemble. The quality control performed in terms of the effective ensemble size, on the contrary, provided with decrease in the RMSE and lower error than ensemble Kalman filter. We observed that EnSRF is also dependent on the quality of initial guess at small ensemble sizes though as the ensemble size increases EnSRF becomes robust. Therefore in future work, we plan to examine the performance of EnTPF with a smoother transition from the prior to posterior distribution.

Acknowledgments

This work is part of the research programme Shell-NWO/FOM Computational Sciences for Energy Research (CSER) with project number 14CSER007 which is partly financed by the Netherlands Organization for Scientific Research (NWO).

References

[1] Sigurd I Aanonsen, Geir Nævdal, Dean S Oliver, Albert C Reynolds, Brice Vallès, et al. The ensemble kalman filter in reservoir engineering–a review. *Spe Journal*, 14(03):393–412, 2009.

[2] Jeffrey L Anderson and Stephen L Anderson. A monte carlo implementation of the nonlinear filtering problem to produce ensemble assimilations and forecasts. *Monthly Weather Review*, 127(12):2741–2758, 1999.

[3] Yan Chen and Dongxiao Zhang. Data assimilation for transient flow in geologic formations via ensemble kalman filter. *Advances in Water Resources*, 29(8):1107–1122, 2006.

[4] Yuan Cheng and Sebastian Reich. Assimilating data into scientific models: An optimal coupling perspective. In *Nonlinear Data Assimilation*, pages 75–118. Springer, 2015.

[5] Mike Christie, Vasily Demyanov, and Demet Erbas. Uncertainty quantification for porous media flows. *Journal of Computational Physics*, 217(1):143–158, 2006.

[6] Laura Dovera and Ernesto Della Rossa. Multimodal ensemble kalman filtering using gaussian mixture models. *Computational Geosciences*, 15(2):307–323, 2011.

[7] Richard E Ewing, Michael S Pilant, J Gordon Wade, and A Ted Watson. Estimating parameters in scientific computation: A survey of experience from oil and groundwater modeling. *IEEE Computational Science & Engineering*, 1(3):19–31, 1994.

[8] Gregory Gaspari and Stephen E Cohn. Construction of correlation functions in two and three dimensions. *Quarterly Journal of the Royal Meteorological Society*, 125(554):723–757, 1999.

[9] Nævdal Geir, Liv Merethe Johnsen, Sigurd Ivar Aanonsen, Erlend H Vefring, et al. Reservoir monitoring and continuous model updating using ensemble kalman filter. In *SPE Annual Technical Conference and Exhibition*. Society of Petroleum Engineers, 2003.

[10] Michael Ghil and Paola Malanotte-Rizzoli. Data assimilation in meteorology and oceanography. *Advances in geophysics*, 33:141–266, 1991.

[11] Plaza Guingla, Douglas Antonio, Robain De Keyser, Gabriëlle De Lannoy, Laura Giustarini, Patrick Matgen, and Valentijn Pauwels. The importance of parameter resampling for soil moisture data assimilation into hydrologic models using the particle filter. *Hydrology and Earth System Sciences*, 16(2):375–390, 2012.

[12] Peter L Houtekamer and Herschel L Mitchell. Ensemble kalman filtering. *Quarterly Journal of the Royal Meteorological Society*, 131(613):3269–3289, 2005.

[13] Brian R Hunt, Eric J Kostelich, and Istvan Szunyogh. Efficient data assimilation for spatiotemporal chaos: A local ensemble transform kalman filter. *Physica D: Nonlinear Phenomena*, 230(1):112–126, 2007.

[14] Marco A Iglesias, Kody JH Law, and Andrew M Stuart. Ensemble kalman methods for inverse problems. *Inverse Problems*, 29(4):045001, 2013.

[15] Andrew H Jazwinski. Stochastic processes and filtering theory, acad. *Press, New York*, 1970.

[16] MV Krymskaya, RG Hanea, and M Verlaan. An iterative ensemble kalman filter for reservoir engineering applications. *Computational Geosciences*, 13(2):235–244, 2009.

[17] Rolf J Lorentzen, Kjell Kåre Fjelde, Johnny Frøyen, Antonio CVM Lage, Geir Nævdal, Erlend H Vefring, et al. Underbalanced drilling: Real time data interpretation and decision support. In *SPE/IADC drilling conference*. Society of Petroleum Engineers, 2001.

[18] Carsten Montzka, Hamid Moradkhani, Lutz Weihermüller, Harrie-Jan Hendricks Franssen, Morton Canty, and Harry Vereecken. Hydraulic parameter estimation by remotely-sensed top soil moisture observations with the particle filter. *Journal of Hydrology*, 399(3):410–421, 2011.

[19] Hamid Moradkhani, Soroosh Sorooshian, Hoshin V Gupta, and Paul R Houser. Dual state–parameter estimation of hydrological models using ensemble kalman filter. *Advances in water resources*, 28(2):135–147, 2005.

[20] Dean S Oliver and Yan Chen. Recent progress on reservoir history matching: a review. *Computational Geosciences*, 15(1):185–221, 2011.

[21] Dean S Oliver, Luciane B Cunha, and Albert C Reynolds. Markov chain monte carlo methods for conditioning a permeability field to pressure data. *Mathematical Geology*, 29(1):61–91, 1997.

[22] Dean S Oliver, Albert C Reynolds, and Ning Liu. *Inverse theory for petroleum reservoir characterization and history matching*. Cambridge University Press, 2008.

[23] Suhas Patankar. *Numerical heat transfer and fluid flow*. CRC press, 1980.

[24] Ofir Pele and Michael Werman. Fast and robust earth mover's distances. In *Computer vision, 2009 IEEE 12th international conference on*, pages 460–467. IEEE, 2009.

[25] Justyna K Przybysz-Jarnut, Remus G Hanea, Jan-Dirk Jansen, and Arnold W Heemink. Application of the representer method for parameter estimation in numerical reservoir models. *Computational Geosciences*, 11(1):73–85, 2007.

[26] Sebastian Reich and Colin Cotter. *Probabilistic forecasting and Bayesian data assimilation*. Cambridge University Press, 2015.

[27] Rolf H Reichle, Dennis B McLaughlin, and Dara Entekhabi. Hydrologic data assimilation with the ensemble kalman filter. *Monthly Weather Review*, 130(1):103–114, 2002.

[28] Albert C Reynolds, Nanqun He, Lifu Chu, Dean S Oliver, et al. Reparameterization techniques for generating reservoir descriptions conditioned to variograms and well-test pressure data. *SPE Journal*, 1(04):413–426, 1996.

[29] Gilbert Strang and Kaija Aarikka. *Introduction to applied mathematics*, volume 16. Wellesley-Cambridge Press Wellesley, MA, 1986.

[30] Sam Subbey, Michael Christie, and Malcolm Sambridge. Prediction under uncertainty in reservoir modeling. *Journal of Petroleum Science and Engineering*, 44(1):143–153, 2004.

[31] Michael K Tippett, Jeffrey L Anderson, Craig H Bishop, Thomas M Hamill, and Jeffrey S Whitaker. Ensemble square root filters. *Monthly Weather Review*, 131(7):1485–1490, 2003.

[32] Peter Jan van Leeuwen. Nonlinear data assimilation in geosciences: an extremely efficient particle filter. *Quarterly Journal of the Royal Meteorological Society*, 136(653):1991–1999, 2010.

[33] Erlend H Vefring, Gerhard H Nygaard, Rolf J Lorentzen, Geir Naevdal, Kjell K Fjelde, et al. Reservoir characterization during underbalanced drilling (ubd): methodology and active tests. *SPE Journal*, 11(02):181–192, 2006.

[34] AT Watson, JG Wade, and RE Ewing. Parameter and system identification for fluid flow in underground reservoirs. In *Proceedings of the Conference Inverse Problems and Optimal Design in Industry*, pages 81–108. Springer, 1994.

[35] Albrecht H Weerts and Ghada YH El Serafy. Particle filtering and ensemble kalman filtering for state updating with hydrological conceptual rainfall-runoff models. *Water Resources Research*, 42(9), 2006.

[36] Mohammad Zafari, Albert Coburn Reynolds, et al. Assessing the uncertainty in reservoir description and performance predictions with the ensemble kalman filter. In *SPE Annual Technical Conference and Exhibition*. Society of Petroleum Engineers, 2005.